Research Article

Stefano Invernizzi, Amedeo Manuello Bertetto*, Federico Ciaccio, and Paolo Nicola

Design of a modular exhibition structure with additive manufacturing of eco-sustainable materials**

https://doi.org/10.1515/cls-2021-0019
Received Sep 30, 2020; accepted Jan 15, 2021

Abstract: In this paper the mechanical characteristics of an innovative bioplastic material, the HBP® - HempBioPlastic® filament, is investigated. HBP® was recently patented by an Italian company Kanésis that focused its activity on nature-derived materials. The filaments are the upshot of an original process allowing to reuse the surplus of the agricultural supply chains and transform it into new sustainable materials. At first, the 3D printed HBP® samples were tested in tensile tests according to the ASTM-D638 standard and monitored in term of deformations by the Digital Image Correlation techniques (DIC) in order to evaluate the stress-strain behavior of different HBP® textures under loading. In addition, using the HBP® and the results coming from the experimental campaign, the design of an exhibition pavilion was proposed. The pavilion was modelled starting from the geometric construction of the fullerene. The supporting modular structure is combined by HBP® modular elements, that can be produced by 3D printing or moulding. Finally, in order to demonstrate the feasibility of the proposed pavilion, a linear finite element analysis is presented on the base of the experimentally determined mechanical properties of HBP® elements, under the effects of wind and seismic environmental actions.

Keywords: hemp bio plastic, additive manufacturing, fused deposition, modelling, green building

1 Introduction

In the construction field plastic materials are now widely used thanks to their characteristics and properties over other materials such as concrete, metals, wood and rocks [1]. Worldwide annual plastics production is considered more than 300 million tons during the last ten years, an important part is devoted to architecture and building uses [2]. Since plastics are used in a large number of applications, environmental problems related to plastic production and disposal emerged drastically. The main environmental concern is related to the location and the dimension of dumps [3]. The amounts of plastic waste appeared as a disaster in many areas of the world because of landfill capacity, rising costs and strong legislature impositions [1–3]. Other, specific environmental problems are related to the accretion of plastics in oceans. For example, in a long-term study, one oceanic seawater sample contained the equivalent of $580{\times}10^3$ plastic fragments per square kilometer [4]. At the same time, plastic burning generates toxic emissions. Today, these GHGs (greenhouse gases) contribute to climate change all over the world [5]. An additional problematic of plastic use in construction is their durability. Plastic is not biodegradable and will persist in the environment for hundreds of years [6].

In recent times, these environmental/economic problems and social concerns have triggered developing environmentally friendly materials such as bioplastics [7]. Bioplastics are novel materials of the 21st century and would be of great importance to the materials world [8]. Bioplastic production and consumption will grow bigger in the future in the world. Because of this, these materials need to be evaluated carefully for sustainability and waste management. Therefore, in the present paper, a deep study on performance of bioplastics materials, focusing on benefits or disadvantages of bioplastics for structural employments is proposed. The use of bioplastic in architecture and design

***Corresponding Author: Amedeo Manuello Bertetto:** Department of Structural, Geotechnical and Building Engineering, Politecnico di Torino – Torino, Italy; Email: amedeo.manuellobertetto@polito.it
Stefano Invernizzi, Federico Ciaccio: Department of Structural, Geotechnical and Building Engineering, Politecnico di Torino – Torino, Italy
Paolo Nicola: Laboo s.r.l., Via Municipio, 165, 95045 Misterbianco (CT) - Italy. Via Mignano 26 – Solagna (Vi), Italy

** Paper included in the Special Issue entitled: Shell and Spatial Structures: Between New Developments and Historical Aspects

was recently suggested in several case-studies and applications [9, 10]. Current uses of agricultural residue-based biocomposites have proven the advantages of natural fibres (agro-fibres) as a basis for a new series of high-quality, recyclable, and environmentally friendly building materials in contemporary architecture [10]. In 2013, supported by the European Regional Development Fund (EFRE), a pavilion named Arboskin was constructed on the campus of the University of Stuttgart featuring a bioplastic façade – a hybrid mixture of non-reinforced bioplastics such as polylactide (PLA), lignin, starch, polyester, waxes, and others. The semi-finished sheets served as cladding for flat or free-formed interior and exterior walls. The material can be recycled and meets the high durability and inflammability standards for building materials [10]. In the present study, the purpose was to design a typology of habitable module that could be easy to be produce, to transported, building a lightweight structure perfectly related to the environmental standards. These assumptions push us to follow the design approaches proposed by the R. B. Fuller and J. Prouve' works (1950-1980). This kind of architecture was influenced by industrial thinking and prefabrication systems. Architecture that demonstrates a functionalist approach related to the environment and the self-sufficiency od the structure. In this way, it was decided to design an exhibition pavilion constituted by compostable and recyclable materials and based on the fullerene framework. The aim of using eco-sustainable materials allowed us to investigate the new uses of vegetal fibre added with different types of matrix layouts.

To investigate the bioplastic mechanical properties for its use as a structural material in the construction field, specific tests on the 3D-printed HBP® samples were conducted at the Department of Structural, Geotechnical and Building Engineering of the Politecnico di Torino (Italy). The 3D printed HBP® samples were tested in tensile tests according to the ASTM-D638 standard and monitored in term of deformations by DIC in order to evaluate the stress-strain behavior of different HBP® textures under loading.

The experimental campaign was realized in collaboration with Kanésis, an innovative Italian start-up company that, in 2014, started to use the wooden part of the hemp plant (shives) combined with the polymer PLA (polylactic acid, derived from maize starch) to produce a 3D printable filament patented with the name of HBP®-Hemp Bio Plastic®. The HBP® filament incorporates different interesting aspects that allow to consider it a valid ecological substitute. These are the environmental benefits due to the hemp cultivation, the easy availability of raw materials, the low energy production and the possibility to compost it. At this moment, this biopolymer is used by the company to produce only small decorative or daily use objects, but the mechanical properties resulting from the experimental campaign suggested that this new eco-friendly material can also be used to produce structural frames and buildings, in an innovative and sustainable way.

2 Experimental procedure and specimen production

To investigate the HBP®-HempBioPlastic mechanical properties for its use as structural material, specific tests on the 3D-printed specimens in the laboratory were performed. The specimen were printed with the 3D printer TEVO (www.tevousa.com) model TORNADO, controlled by the software Ultimaker Cura 4.4 (www.ultimaker.com). As Kuznetsov affirmed in [11], there are no set standards for testing the specimens produced by FDM-Fused Deposition Modeling technology. Taking into account of this condition and the experiences of other researchers [12–16], the ASTM-D638 e [17] was followed to try out with tensile tests the biopolymer. The tensile test took place at the DISEG (Department for Structural and Geotechnical Engineering) laboratory of Polytechnic of Turin (Italy). The temperature and the humidity of the laboratory have been maintained respectively at 23°C and 50%, as recommended by ASTM-D638-14 [17].

The tests were conducted by the ZWICK/Roell-Z050 equipment with a test constant velocity of 5 mm/min (Figure 1a). For some specimens, the DIC-Digital Image Correlation analysis has been applied using the DIC System Q-400 equipment and filmed in 200 fps with the GoPro-HERO5, especially around the breaking point of the specimens.

The specimens are characterized by a smooth surface (in contact with the print bed) with two oblique lines and a rougher one on the opposite side. During the experimental campaign, 27 of 35 specimens were tested up to the final

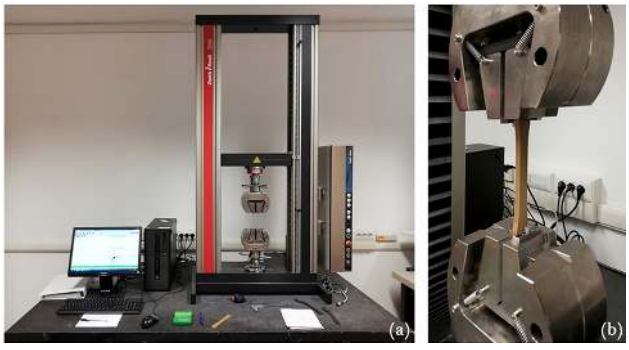

Figure 1: Experimental set-up: (a) ZWICK/Roell-Z050 equipment, (b) positioning of the specimens during the tensile tests

failure condition. The placement of the specimens inside the clamps is a griping extension of 20 mm for each side as reported in Figure 1b.

The software equipment provided the stress-strain curve for each specimen tested and the values achieved permitted us to obtain the values required by the technical rules and described below [17]: The tensile Strength (σ_t) was calculated by the ratio between the maximum load sustained by the specimen [N] and the average original cross-sectional area in the gauge length (S_{cs}) [mm^2]: $\sigma_t = F_{max}/S_{cs}$. At the same time the percent elongation at the yielding point (P_{eY}): is calculated during the test as the change in the gauge length respect to the original specimen gauge length. Similarly, the elongation at the break point (P_{eB}) is the change in length in correspondence of the specimen failure respect to the original specimen length. In Table 1 and in Figure 2 the dimensions of the specimens are reported.

Table 1: Specimens characteristics relative ASTM-D638

Symbol	Description	Measure [mm]
W	Width of narrow cross section	13.00
L	Length of narrow cross section	57.00
WO	Overall width	19.00
LO	Overall length	165.00
G	Gauge length c	50.00
D	Distance between clamps	115.00
R*	Rounding-off radius	141.67
T	Thickness	7.00

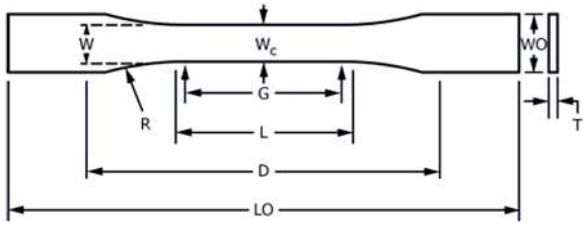

Figure 2: ASTM-D638, type I: dimensions [17]

The ASTM-D638 offered five typologies of specimens, each of them characterized by different dimensions. The "Type I" has been chosen for the test considering the production standards offered by the company Kanésis. Thus, keeping the original size of the specimens, a parabolic profile was proposed, continuous and tangent to the shorter section. The Italian start-up Kanésis printed the HBP® specimen (code: PLA A/17 NAT) by the 3D-printer in order to produce 5 specimens for each type.

In this case, the total amount of 35 specimens was produced. Table 3 summarized the physical characteristics and the moulding parameters of each tested specimen. The variable values in term of weight and volume permitted to define 7 different sets of specimens, named with the letters from A to G. Among the characterizing parameters for each set we have also the orientation and the raster configuration of the layers.

For all the classes, the orientation is set to 0° on the XY print bed except for the B class that presented the specimens orientated of 45°/−45° on the print bed.

The raster or infill configuration represented the internal structure of the specimen. Concerning this setting the most interesting configurations were chosen for each typology of 2D structure and 3D structure. These factors allow us to understand how these characteristics influenced the mechanical properties of the tested specimens. All the infill configurations are briefly described below and showed in Figure 3.

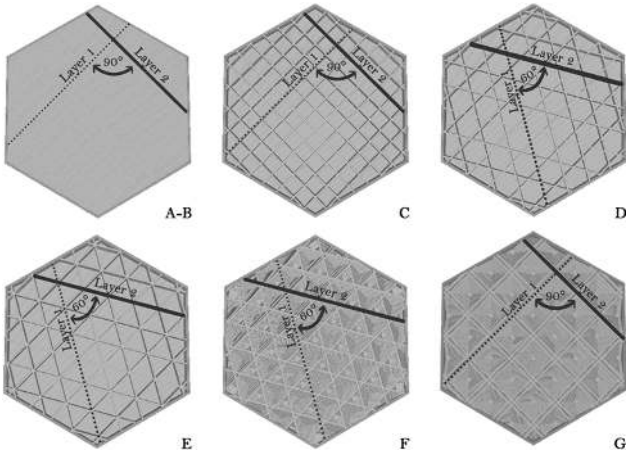

Figure 3: Infill structure schemes for Types A-G. Note that x and y reference of the printing bed correspond to horizontal and vertical directions in the figure respectively

The 2D structure category presented all the infill configurations constituted by perfectly overlaid layers without any variation of the "air gap" (void between filaments). Every layer is different from the others just for the opposite print direction. For the specimens A and B the texture consists of the filament positioned with a negative air gap. It covered all the specimen surface, and each layer is rotated of 90° respect the previous one. The specimen belonging to the type C presented the same design of A and B types but the air gap is greater than 0. The texture, in this case, appeared composed by squares. The specimens of Tri-Hexagon type (D) are characterized by a filling formed by a

Table 2: Values of the specimens' physics characteristics and print settings

SPECIMEN CODE		CHARACTERISTICS			PRINT PARAMETERS									
		Weight [g]	Volume [m³]	Density [kg/m³]	Orientation [°]	Layer height [mm]	Nozzle diameter [mm]	Infill [%]	Air Gap [mm]	Raster angle [°]	Raster configuration [-]	Contour width [mm]	Number of shell [-]	Flow rate [%]	Printing temperature [°C]
2D STRUCTURE	1(1)	12.032	1.78E−05	676.13	0	0.20	0.80	100	−0.05	0; 90	Lines	3.50	2	100	175/200
	2(2)	12.038	1.78E−05	676.46	0	0.20	0.80	100	−0.05	0; 90	Lines	3.50	2	100	175/200
A	3(3)	11.994	1.78E−05	673.99	0	0.20	0.80	100	−0.05	0; 90	Lines	3.50	2	100	175/200
	4(4)	11.950	1.78E−05	671.52	0	0.20	0.80	100	−0.05	0; 90	Lines	3.50	2	100	175/200
	5(5)	11.860	1.78E−05	666.46	0	0.20	0.80	100	−0.05	0; 90	Lines	3.50	2	100	175/200
	1(6)	11.876	1.78E−05	667.36	45	0.20	0.80	100	−0.05	0; 90	Lines	3.50	2	100	175/200
	2(7)	11.954	1.78E−05	671.74	45	0.20	0.80	100	−0.05	0; 90	Lines	3.50	2	100	175/200
B	3(8)	11.542	1.78E−05	648.59	45	0.20	0.80	100	−0.05	0; 90	Lines	3.50	2	100	175/200
	4(9)	11.759	1.78E−05	660.78	45	0.20	0.80	100	−0.05	0; 90	Lines	3.50	2	100	175/200
	5(10)	11.607	1.78E−05	652.24	45	0.20	0.80	100	−0.05	0; 90	Lines	3.50	2	100	175/200
	1(11)	10.870	1.78E−05	610.83	0	0.20	0.80	25	3.20	0; 90	Grid	3.50	2	100	175/200
	2(12)	11.194	1.78E−05	629.04	0	0.20	0.80	25	3.20	0; 90	Grid	3.50	2	100	175/200
C	3(13)	11.347	1.78E−05	637.63	0	0.20	0.80	25	3.20	0; 90	Grid	3.50	2	100	175/200
	4(14)	11.320	1.78E−05	636.12	0	0.20	0.80	25	3.20	0; 90	Grid	3.50	2	100	175/200
	5(15)	11.334	1.78E−05	636.90	0	0.20	0.80	25	3.20	0; 90	Grid	3.50	2	100	175/200
	1(16)	14.186	1.78E−05	797.17	0	0.20	0.80	88	2.65	0; 60	Tri-Hexagon	3.50	2	75	175/200
	2(17)	13.702	1.78E−05	769.97	0	0.20	0.80	88	2.65	0; 60	Tri-Hexagon	3.50	2	75	175/200
D	3(18)	13.736	1.78E−05	771.88	0	0.20	0.80	88	2.65	0; 60	Tri-Hexagon	3.50	2	75	175/200
	4(19)	14.131	1.78E−05	794.08	0	0.20	0.80	88	2.65	0; 60	Tri-Hexagon	3.50	2	75	175/200
	5(20)	14.074	1.78E−05	790.87	0	0.20	0.80	88	2.65	0; 60	Tri-Hexagon	3.50	2	75	175/200
	1(21)	14.951	1.78E−05	840.16	0	0.20	0.80	88	2.65	0; 60	Triangles	3.50	2	75	175/200
	2(22)	14.941	1.78E−05	839.59	0	0.20	0.80	88	2.65	0; 60	Triangles	3.50	2	75	175/200
E	3(23)	14.888	1.78E−05	836.62	0	0.20	0.80	88	2.65	0; 60	Triangles	3.50	2	75	175/200
	4(24)	14.762	1.78E−05	829.54	0	0.20	0.80	88	2.65	0; 60	Triangles	3.50	2	75	175/200
	5(25)	14.601	1.78E−05	820.49	0	0.20	0.80	88	2.65	0; 60	Triangles	3.50	2	75	175/200

Table 2: ...continued

SPECIMEN CODE		CHARACTERISTICS			PRINT PARAMETERS									
		Weight	Volume	Density	Orientation	Layer height	Nozzle diameter	Infill	Air Gap	Raster angle	Raster configuration	Contour width	Number of shell	Flow rate	Printing temperature
		[g]	[m^3]	[kg/m^3]	[°]	[mm]	[mm]	[%]	[mm]	[°]	[-]	[mm]	[-]	[%]	[°C]
3D STRUCTURE	1(26)	13.916	1.78E−05	782.00	0	0.20	0.80	88	variable	0; 60	Cube	3.50	2	75	175/200
	2(27)	14.045	1.78E−05	789.24	0	0.20	0.80	88	variable	0; 60	Cube	3.50	2	75	175/200
F	3(28)	13.974	1.78E−05	785.25	0	0.20	0.80	88	variable	0; 60	Cube	3.50	2	75	175/200
	4(29)	14.033	1.78E−05	788.57	0	0.20	0.80	88	variable	0; 60	Cube	3.50	2	75	175/200
	5(30)	14.190	1.78E−05	797.39	0	0.20	0.80	88	variable	0; 60	Cube	3.50	2	75	175/200
	1(31)	11.298	1.78E−05	634.88	0	0.20	0.80	60	variable	0; 90	Octagonal	3.50	2	75	175/200
	2(32)	11.660	1.78E−05	655.22	0	0.20	0.80	60	variable	0; 90	Octagonal	3.50	2	75	175/200
G	3(33)	11.438	1.78E−05	642.75	0	0.20	0.80	60	variable	0; 90	Octagonal	3.50	2	75	175/200
	4(34)	11.262	1.78E−05	632.86	0	0.20	0.80	60	variable	0; 90	Octagonal	3.50	2	75	175/200
	5(35)	11.573	1.78E−05	650.33	0	0.20	0.80	60	variable	0; 90	Octagonal	3.50	2	75	175/200

Table 3: Results from the tensile test according to the ASTM-D638 standard

specimen class		$Load_{max}$ [N]	ΔL Break [m]	Tensile Strength [Pa]	Percent Elongation at Yield [%]	Percent Elongation at Break [%]
A	Average	883.86	1.44E−03	9.78E+06	0.84	0.88
	St. Dev.	40.31	1.22E−04	4.46E+05	0.08	0.07
B	Average	758.36	1.58E−03	8.39E+06	0.95	0.96
	St. Dev.	38.53	3.15E−05	4.26E+05	0.02	0.02
C	Average	712.83	1.29E−03	7.89E+06	0.77	0.78
	St. Dev.	30.66	6.92E−05	3.39E+05	0.04	0.04
D	Average	992.91	1.28E−03	1.10E+07	0.76	0.78
	St. Dev.	28.08	6.68E−05	3.11E+05	0.04	0.04
E	Average	1037.74	1.33E−03	1.15E+07	0.78	0.81
	St. Dev.	54.42	6.46E−05	6.02E+05	0.03	0.04
F	Average	1193.70	2.45E−03	1.32E+07	1.17	1.27
	St. Dev.	23.56	8.19E−04	2.61E+05	0.09	0.15
G	Average	846.11	1.83E−03	9.36E+06	1.07	1.11
	St. Dev.	73.62	7.19E−05	8.15E+05	0.03	0.04

structure of triangles and hexagons. This texture is possible because every layer shifted and rotated of 60° respect the previous one. The last typology belonging to 2D-structure is characterized by the Triangles texture (E). This is constituted by equilateral triangles obtained by layers rotated of 60° (Figure 3).

Finally, the 3D Structure is reported. The infill structures of this category are different from the previous ones because here the air gap changed in all layers along the thickness of the specimen (Z-axis direction). This peculiarity permitted a honeycomb internal structures of the specimen (types F and G).

In particular, the Cube type (F) consisted of the same concept of the "Tri-Hexagon" configuration but the variation of the "air gap" permitted the formation of close cells. The Octagonal type (G) is based on the "Grid" design presenting closed cells thanks to the air gap variation. From measurement operations, the "Grid" configuration produced the lightest specimens with an average density of 630.10 Kg/m^3, the heaviest ones are obtained by the "Triangles" typology configuration with an average density of 833.28 Kg/m^3.

In the following Sections, the mechanical behavior of the 3D printed or injection molded HBP® material will be preliminarily assumed as homogeneous and isotropic. Actually, further studies will be mandatory to assess the anisotropic behavior of the material, which depends also on the deposition texture, by means of multi-axial tests. In addition, the deposition path of the final elements should be explicitly accounted for in the eventual anisotropic material numerical simulation. Moreover, the reticulated nature of the deposed infill is likely prone to local instabilities when subjected to compression. Therefore compressive test will be necessary in the future to assess the mechanical behavior in compression.

3 Digital Image Correlation analysis of the HBP® specimens

The Digital Image Correlation (DIC) is an optic method based on the correlation of both 2D and 3D digital image taken in different steps [19–22]. This method allows to determinate the modification and the deformations of the specimen. It is widely used in different science and engineering applications. The amount of information and data about the deformation obtained during the mechanical test is compared to the strain-gauge output of the ZWICK/Roell-

Z050 equipment and the information obtained by local and larger data using the digital image acquisition [23–28].

The DIC analysis performed in this work estimated the HBP® specimen response during the tensile test. In particular, the specimen deformations are individuated by the DIC device with a series of frames that involving the tracing of every texture of the specimens.

In Figure 4a the specimen F5(30) with the speckled texture applied on it is reported. This texture is formed by a first homogeneous layer of white acrylic paint and a second pattern applied by spraying reproducing a cloud of points with the target function.

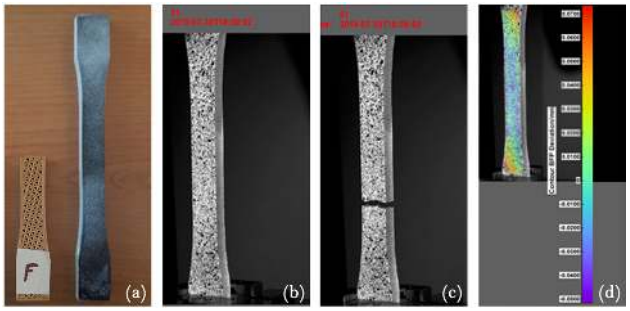

Figure 4: HBP® specimen F5(30): (a) Acrylic layer applied (b) STEP 1 (starting test); (c) STEP 51 (collapse condition); (d) Distance to best fit plane

The DIC System Q-400 (Dantec Dynamics A/S) [18] and the 3D-DIC software have been used to evaluate the deformation curves. The correlation algorithm adopted is based on the tracking of grey value pattern in small local neighborhoods. Being $G(x,y)$ the grey value of a pixel pattern with the coordinate x and y inside of the subset or facet, the correlation algorithm minimizes the sum:

$$\sum_{x,y} (G_t(x_t, y_t) - G(x, y))^2 \quad (1)$$

where $G_t(x_t, y_t) = g_0 + g_1 G(x_t, y_t)$ and $x_1 = a_0 + a_1 x + a_2 y + a_3 xy$ and $y_1 = a_4 + a_5 x + a_6 y + a_7 xy$. By the variation of the illumination parameters (g_0, g_1) and the parameters of the similarity transformation $(a_0 \ldots a_7)$ an accuracy for the matching of better than 0.01 pixel can be achieved. The correlation algorithm which is actually applied is a two dimensional generalization of the case just described. It implies, in particular, a two dimensional geometric transformation which is to rectify perspective distortion and relief displacement. In view of the small size of the image areas it is sufficient to apply affine linear transformation (six a type parameters) [29]. Once the 3D contour has been determined, the second step in digital 3D correlation is the measurement and the determination of the three-dimensional deformation of the object surface (deformed pattern). This process is carried out by correlation of the images, taken by both cameras respect to their original reference images. In Figure 4d. DIC application is shown together with the experimental set-up. It is possible to note the F5(30) specimen in its initial test (Figure 4b) and collapsed situations (Figure 4c).

Table 3 and in Figure 5 the average stress-deformation average results from tensile tests are reported. At the beginning of the experiments, it is possible to notice some changes related to the constraint conditions inside the specimens. The curves have different values, but their path is similar to each other and it reflects the behavior of a thermoplastic material. In Figure 6 a comparison of specimen classes with Percent Elongation at Break is reported. The largest tensile strength value obtained is 1.36e+07 Pa

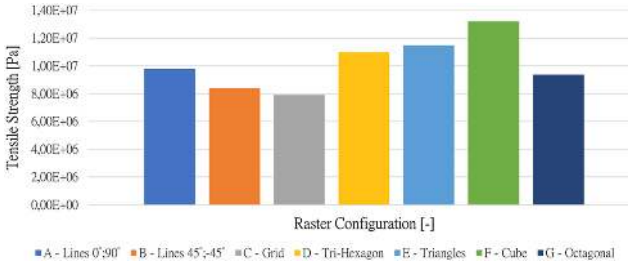

Figure 5: Comparison of specimen classes with Tensile Break [Pa]

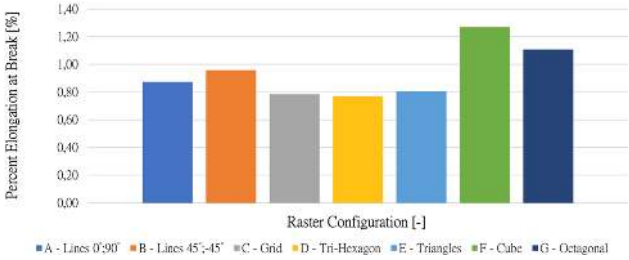

Figure 6: Comparison of specimen classes with Percent Elongation at Break [%]

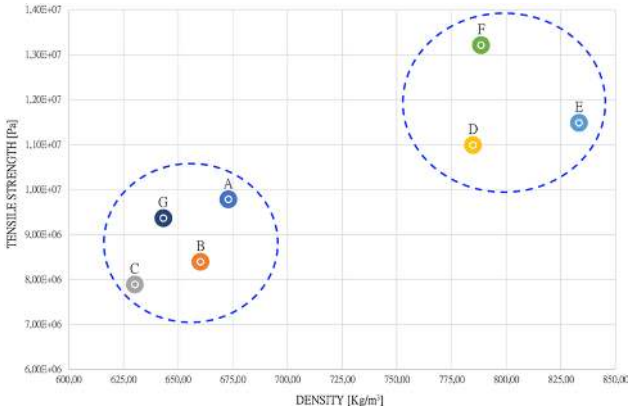

Figure 7: Graph of Tensile Strength/Density correlation

of the specimen F2(27), the highest deformation at break is 2.44 mm of the specimen F5(30). As far as the average tensile strength is concerned, the decreasing order is for each set of specimen is: F-type with $1.32\times10^{+07}$ Pa, E-type with $1.15\times10^{+07}$ Pa, D-type with $1.10\times10^{+07}$ Pa, A-type with $9.78\times10^{+06}$ Pa, G-type with $9.36\times10^{+06}$ Pa, B-type with $8.39\times10^{+06}$ and the C-type with $7.89\times10^{+06}$. In term of maximum elongation at the break point, for the F-type is 1.27%, for G-type: 1.11%, B-type: 0.96%, A-type: 0.88%, E-type: 0,81%, C-type: 0.78% and D-type: 0.77%. One of the most important evidence regarded the texture employed for the different specimen sets. Texture with filament along the 0°/90° directions are more performant than the 45°/−45° ones but presented reduced values in the elastic properties.

The density and the tensile strength, as reported in Table 3 and Figure 5, resulted strictly correlated to the infill structure of the specimens. At the same time, it is evident that the different specimen sets can be further subdivided into two fundamental groups: (i) squared grid structure (A, B, C, G) and Triangular grid structure (D, E, F): The first sets (A, B, C, D) occupied the lower portion of the graph in Figure 7 and represented the lighter and the group with the lower tensile strength values. In this group, the C-type is the less performing set and the A-type is the best one. Considering the triangular grid structure (D, E, F), positioned in the higher part of the graph in Figure 7, they presented the most performing infill structures. In this case, the class with the highest density (E-type) do not coincide with the most resistant (F-type). The D-type has the lowest density and tensile strength of this second group.

From these considerations, we can deduce that the quantity of material inside the specimen gave an improvement of the mechanical performance. At the same time, a great contribution is due to the infill structure of the specimen. Looking at the C, G and B classes, they have in common the same structure typology (square grid), but the G-type presented higher tensile strength with reduced

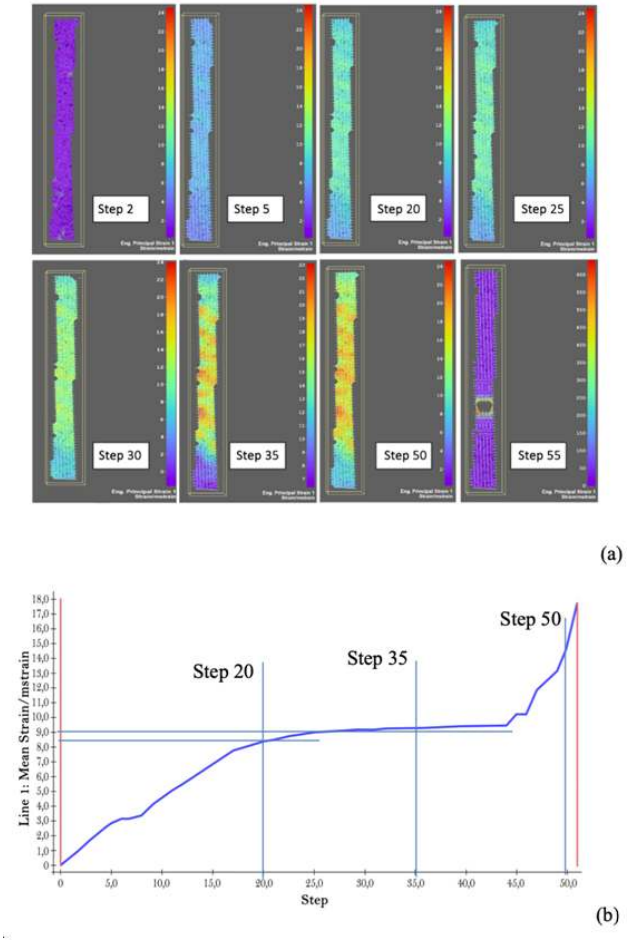

Figure 8: Mean strain versus steps (Time graph). The specimens were subjected to a tensile test until the collapse conditions were reached. Specimen F5(30)

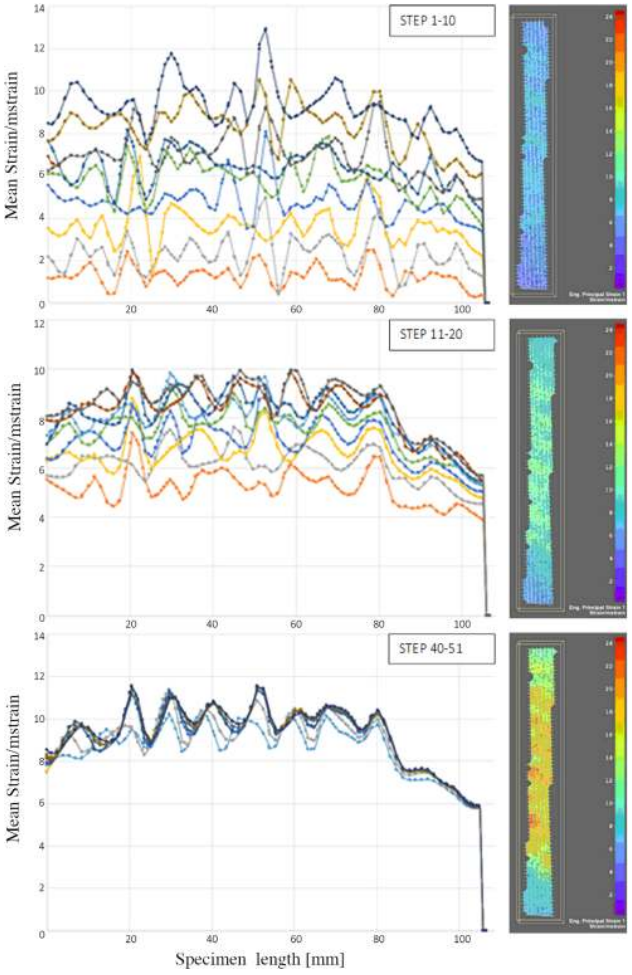

Figure 9: Strain vs Time in different steps. Specimen F5(30)

quantity of material respect to the B-type. Considering the D and F sets, the mechanical performance improvement due to the infill structure is more evident. These two classes have two types of structures with a very similar density, only 4.00 Kg/m^3 of difference, but the F-type is more resistant than the D-type (see Figures 5 and 7 and Table 3).

From the DIC analysis applied to the specimen F5(30), the program obtained the sequence of images reported in Figure 8 and in the graphs in Figure 9 (specimen F5 30). In the first one (Figure 8), it is possible to observe in the central part of the specimen an increasing concentration of the deformation (red portions) localized in oblique bands visible from step 20. In step number 55 the collapse occurred just in correspondence of the highest concentration of the tensile stress. This localization of the stress level is evidenced in the step 50 before that the main crack of the specimen occurred. As it can be seen from the graph shown in Figure 8b, the average deformation of the specimen, considering a line longitudinal to the specimen as a virtual strain gauge, increased, during the first part of the test, up to step 20. Subsequently, there is a reduction of the increasing (stable branch) up to step 35, with the appearance of localized bands of deformation. Subsequently, up to the last step, the average deformation growth very quickly up to collapse (specimen F5 30).

4 Design proposal for an exhibit pavilion in HBP® material

During the last years, the increasing demand for internal distribution flexibility in architecture and the adoption of free forms reticulated structures for large span roofing constructions promoted the use of innovative double curved shells and geodetic structures as a valid solution for column-free spaces and architectures [30, 31]. To this purpose the reticulated, geodetic, lattice or grid shells offer valid innovative possibilities, combining aesthetic tools and structural purposes in a unique solution [32–36]. The fiber reinforced bioplastic material proposed in the present paper, combined with additive manufacturing technologies, appears compatible with the structural use in innovative buildings. Moreover, the results obtained from the experimental campaign, described in the previous Sections, are very promising as far as the structural use of HBP® to realize lightweight structures, geodesic domes and grid shells is concerned [37–40].

The temporary exhibit pavilion was conceived to be compliant with the following performance: adaptability to generic ground conditions; minimal extension of foundations; thermal and acoustic internal comfort; adequate external finishing; dimensional compatibility of the components with respect to the transportation constrains; lightness of components; easiness of assembling; reusability.

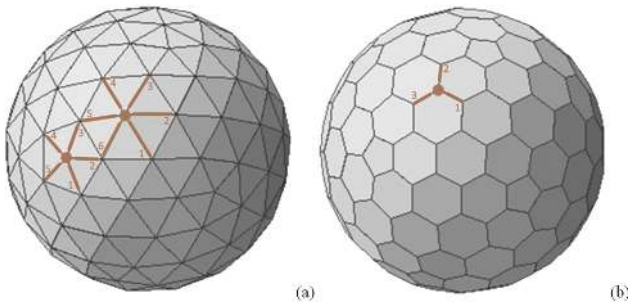

Figure 10: Geodetic dome (a); and dual fullerene polyhedron (b)

The pavilion geometry was inspired by the R. Buckminster Fuller's pioneering geodetic framework based on self-sufficiency and eco-compatibility principles.

The geodetic dome (Figure 10a) is a polyhedron based on icosahedral symmetry and composed of triangles whose vertex, with degree equal to six or five, lays on the same circumscribing sphere. The fullerene (Figure 10b) can be obtained by reduction from the geodetic dome, simply removing the vertexes at the center of pentagons and hexagons. The resulting polyhedron, which is the dual of the geodetic dome, has only vertex with degree equal to three.

Subsequently, pentagons and hexagons are replaced by the corresponding inscribed circumferences, and the obtained structure is truncated at the ground level. As a consequence, the lower incomplete circumferences will serve as the entrances to the pavilion.

The pavilion elevation is equal to 5,26 m, while the maximum diameter in plan is equal to 5,96 m.

Finally, the circumferences are used as director lines to extrude the free-form cross section of the structural frame. The internal volume of the pavilion is around 150 m^3, being the envelope less than 115 m^2. The circular voids of the structure can be left as they are, or covered with opaque or transparent panels, depending on the needs and on the environmental boundary conditions. Opaque panels are made of OBS layers filled with Hemp and Lime. A schematic axonometry of the pavilion with exploded details is shown in Figure 11.

The obtained structural frame can be decomposed into two only modular elements, as shown in Figure 12. As a result, 40 modules A and 10 modules B are necessary to assemble the pavilion.

The modules connection is realized with mortise tenon joints, solidarized by additional pins or screws. The module A footprint is comprised in a 1,36 m by 1,30 m rectangle,

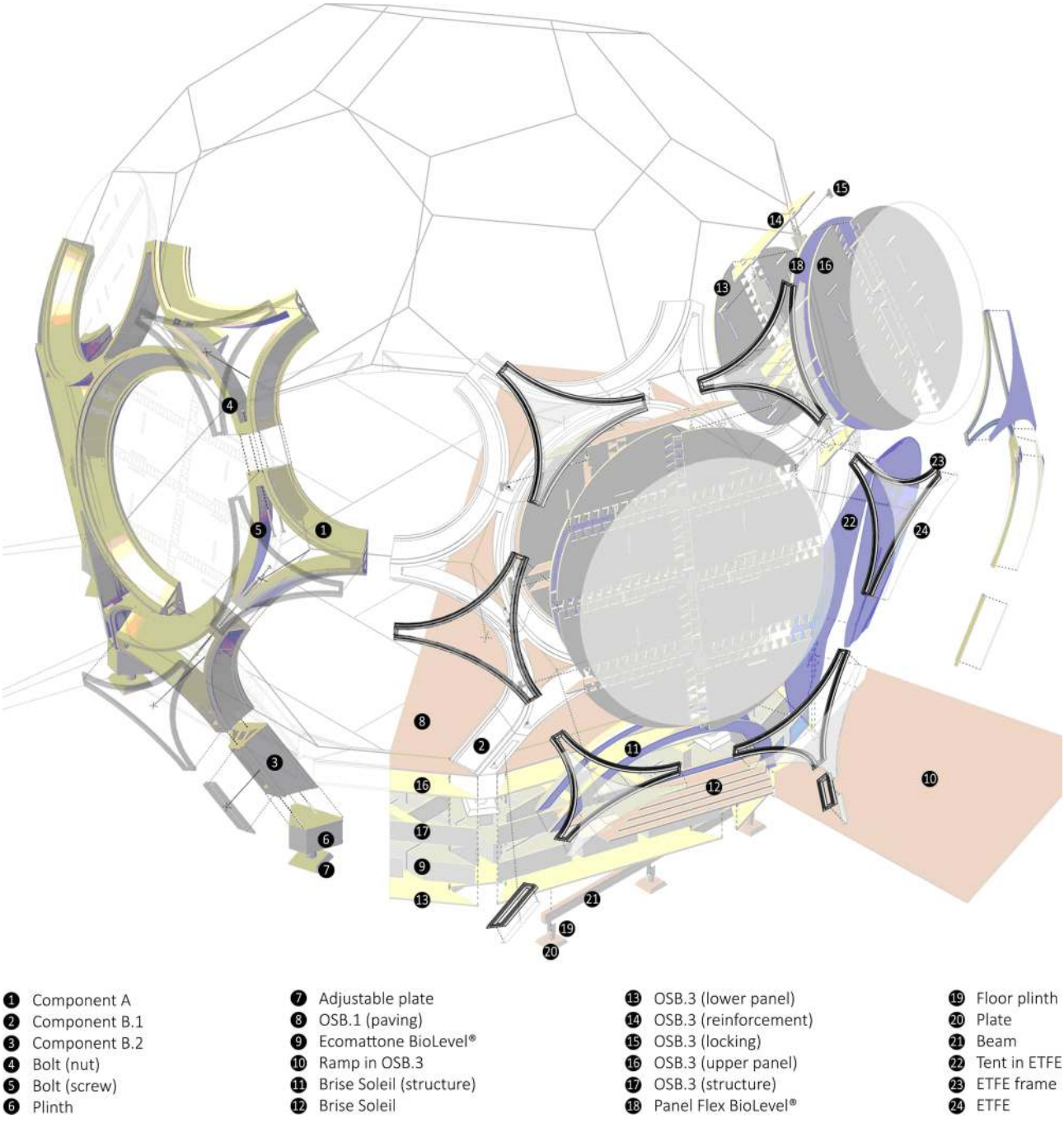

Figure 11: Axonometric exploded view of the exhibit pavilion

allowing for the 3D printing of the modules on nowadays larger 3D printers, or traditional injection molding.

In order to comply with the easiness of assembling requirement, a detailed simulation of the process was carried out, as shown in Figure 13. The designed mounting procedure can be carried out by means of minimal scaffolding, and the eventual help of a movable small crane.

Finally, the structural performance of the structure was preliminarily assessed by means of linear finite element calculations. The dead weight of the structural modules was assumed equal to 9000 N/m^3, which depends both on the density of the base material and on the filling ratio (variable in case of the adopted AM texture or injection molding). The effect of snow (250 daN/m^2) and seismic action (0.3g uniform horizontal acceleration) were accounted for, in addition to permanent loads, in two different load cases (respectively: case 1 and case 2). The seismic action was accounted considering the equivalent static effect of a

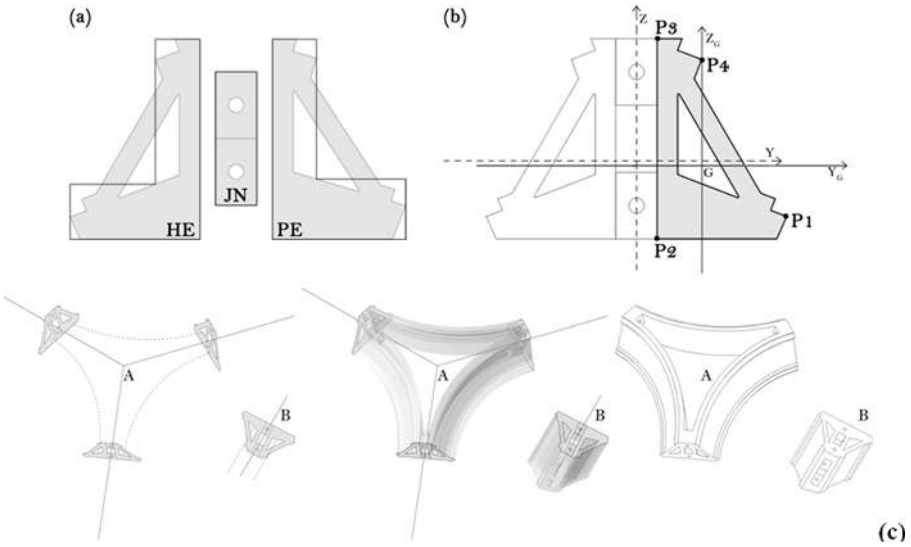

Figure 12: Beam profiles used in the FEM models (in grey) (a); semi-portion of the section (in grey) with the most critical points, where the stresses were assessed (b). Scheme of the modelling phases of the two A and B components (c)

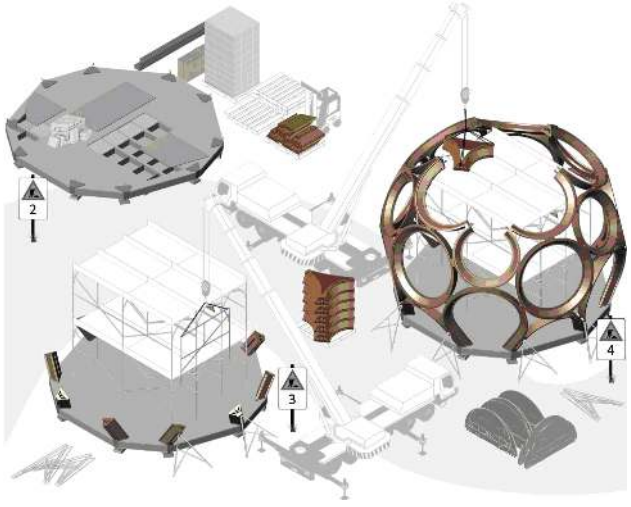

Figure 13: Assembling scheme and organization of the working site

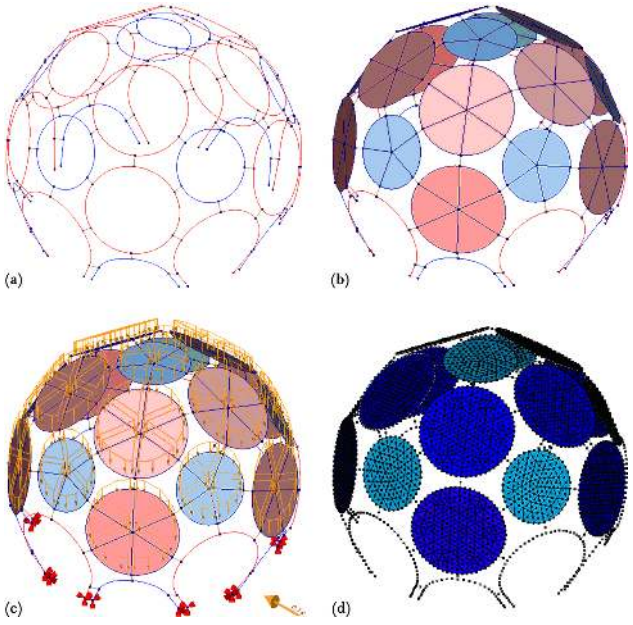

Figure 14: Diana FEA setting phases: (a) Model with all the directions of the structural elements is presented: in red, the hexagon's beams; in blue, pentagonal beams; in black, the junctions; (b) insertion of the infilling surfaces; (c) Complete DIANA model with the application of the snow load and the seismic actions; (d) Output of the calculus obtained by the software

horizontal acceleration equal 0.3 g, where g is the gravity acceleration.

The young modulus was assigned according to the experimental results (E=15GPa). For the sake of simplicity, homogeneous isotropic elastic material was adopted for calculation. The numerical simulations were carried out with the commercial finite element software Diana®. In order to minimize the model complexity, the discretization was carried out by means of numerically integrated beam elements. In order to provide the correct cross section definition (according to Figure 12c), each beam element was equipped with the correct local reference system, where x is the axial curvilinear abscissa, and z is oriented as the normal of the plane which embed each particular circumference. The mechanical behavior of the closure circular panel was represented by triangular shell elements, which served also as loading masks for the distributed loading. The described modelling phases for the finite element model are reassumed in Figure 14.

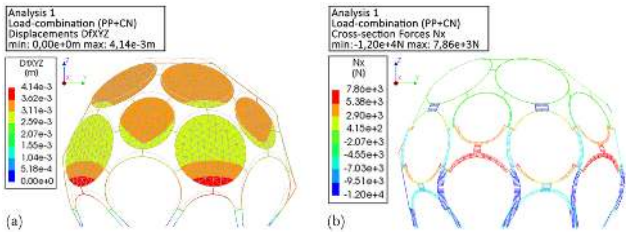

Figure 15: Self-weight and snow (Case 1): (a) Displacement diagram; (b) Normal stress (Nx) diagram

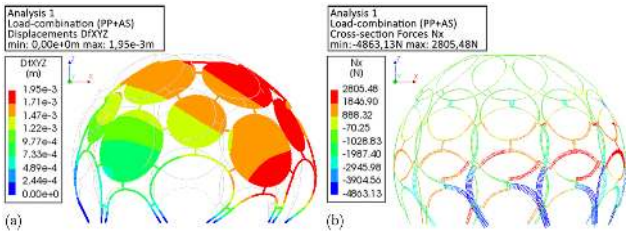

Figure 16: Self-weight and seismic acceleration (Case 2): (a) Displacement diagram; (b) Normal stress (Nx) diagram

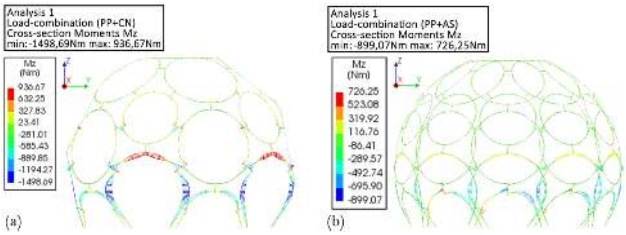

Figure 17: Bending moment diagrams: self-weight and snow (Case 1) (a); self-weight and seismic acceleration (Case 2) (a)

Table 4: Normal stress in the most critical cross section

Pn	σ_z Own Weight [Pa]	σ_z Case 1 [Pa]	σ_z Case 2 [Pa]
P1	9.76E+05	2.88E+06	1.92E+06
P2	1.10E+06	3.22E+06	2.11E+06
P3	5.62E+05	1.76E+06	9.80E+06
P4	8.80E+05	2.59E+06	1.50E+06

The axial force and the displacements diagrams for the two considered load cases are shown in Figure 15 and 16, while the bending moments along the local z axis are shown in Figure 17.

The most stressed cross sections are located, for both the considered load cases, in the lower region of the pavilion structure. Table 3 reports the maximum normal stresses in the four critical points of the most critical cross section (P1-P4) for loading Case 1 and loading Case 2. The highest values are localized in the point P2. The values obtained by the FEM analysis are significantly lower than the tensile strength of the material obtained during the laboratory mechanical tests, which is equal to $1.32E^{+07}$ Pa. In addition, the maximum deformations of the structure under the imposed stresses are of the order of few millimeters, respectively about $4.14E^{-3}$ m for the loading Case 1 and $1.71E^{-3}$ m for the loading Case 2.

On the base of the obtained results, HBP® can be considered a feasible construction material, especially applied to innovative architectures, spatial shells and geodetic structures. The strength limits of HBP®, even in case of additive manufacturing elements, are largely satisfied in the structure considered as the case study. At the same time, further study are needed to verify the behavior of the bioplastic with respect to other loading conditions and, above all, to the phenomena of local and non-local instability, which are crucial in case of light reticular and shells structures [40, 41].

5 Conclusions

In circular economy, bio-based plastics or bioplastics are emerging materials that are increasingly being used in many fields, including packaging, automotive components, biomedical devices, interior design and, last but not least, architecture and constructions.

In the present paper, it has been shown how reinforced bioplastic, and in particular HBP, can be a feasible construction material, especially thanks to additive manufacturing techniques, when applied to innovative space-frame structures and architectures, like the proposed pavilion inspired by geodetic domes.

The experimental campaign, carried out on AM specimens, has put into evidence the crucial role of the infill structure of the specimen, which depends on the adopted deposition scheme. Looking at the C, G and B specimen sets, they have in common the same structure typology (square grid), but the G-type presented higher tensile strength with reduced quantity of material respect to the B-type. Considering the D and F sets, the mechanical performance improvement due to the infill structure is even more evident.

The DIC analysis revealed how, in the central part of the specimens, first the deformation concentration increases, and subsequently it localizes in oblique bands. Finally, the collapse occurs just in correspondence of the highest concentration of the tensile stress. This localization of the stress level is evidenced just before that the main crack of the specimen take place.

In the next experimental campaign also compressive tests will be performed in order to evaluate the behavior of HBP® under high compressive conditions. It is very difficult to imagine the specific behavior of the different patterns due to the compression solicitations also due to the different infill structure schemes

From the obtained results, HBP® appears a very promising material for structural applications to spatial shells and geodetic structures.

Further studies are necessary to verify the conditions of bioplastic and its behavior when subjected to other loading conditions and, above all, in relation to the phenomena of local and non-local instability very frequent in the case of reticular light-weight structures and shells [39, 40]. Many studies have been recently conducted to evaluate both the phenomenon of the so-called coupled instability for shell and spatial structures and the phenomenon of the stiffness of the nodes in the reticulated shell or frame and how it can influence the triggering of instability and collapse phenomena [42–46].

Funding information: The authors state no funding involved.

Author contributions: All authors have accepted responsibility for the entire content of this manuscript and approved its submission.

Conflict of interest: The authors state no conflict of interest.

References

[1] Arikan EB, Duygu HO. 2015 A Review. Investigation of Bioplastics Journal of Civil Engineering and Architecture. 2015;9:188–92.
[2] Alvarez-Chavez CR, Edwards S, Moure-Eraso RL, Geiser K. Sustainability of Bio-based Plastics: General Comparative Analysis and Recommendations for Improvement. J Clean Prod. 2011;23(1):46–7.
[3] Halden RU. Plastics and health risks. Annu Rev Public Health. 2010;31(1):179–94.
[4] Philp JC, Ritchie RJ, Guy K. Biobased plastics in a bioeconomy. Trends Biotechnol. 2013 Feb;31(2):65–7.
[5] Law KL, Morét-Ferguson S, Maximenko NA, Proskurowski G, Peacock EE, Hafner J, et al. Plastic accumulation in the North Atlantic subtropical gyre. Science. 2010 Sep;329(5996):1185–8.
[6] Barker T. Technical Summary in Climate Change 2007: Mitigation. Contribution of Working Group III to the Fourth Assessment. Report of the intergovernmental panel on climate change; 2010
[7] El Kadi S. Bioplastic Production form Inexpensive Sources Bacterial Biosynthesis, Cultivation System, Production and Biodegrability. USA: VDM (Verlag Dr. Müller) Publishing House; 2010
[8] Peelman N, Ragaert P, de Meulenaer B, Adons D, Peeters R, Cardon L, et al. Application of Bioplastics for Food Packaging. Trends Food Sci Technol. 2013;32(2):128–41.
[9] Mohanty AK, Misra M, Drzal LT. Sustainable Bio-composites from Renewable Resources: Opportunities and Challenges in the Green Materials World. J Polym Environ. 2002;10(1-2):19–26.
[10] Hebel DE, Heise F. Cultivated Building Materials. ISBN 978-3-0356-1106-9. https://doi.org/10.1515/9783035608922.
[11] Kuznetov V. E. [et al.]. Strength of PLA Components Fabricated with Fused Deposition Technology Using a Desktop 3D Printer as a Function of Geometrical Parameters of the Process. Polymers (Basel). 2018;313(10).
[12] Cantarell J et al. Experimental Characterization of the Mechanical Properties of 3D-Printed ABS and Polycarbonate Parts. Advancement of Optical Methods in Experimental Mechanics. University of Florida, Gainesville, FL (USA): The Soc Exper Mech. 2016;(3):89–105.
[13] Zou R et al. Isotropic and anisotropic elasticity and yielding of 3D printed material Elsevier. Cina: Elsevier Ltd. Composites Part B. 2016;99:506-513.
[14] Lanzotti A et al. The impact of process parameters on mechanical properties of parts fabricated in PLA with an open-source 3-D printer. Rapid Prototyping J. 2015;5(21):604–17.
[15] Ahn SH et al. Anisotropic material properties of fused deposition modeling ABS. 2002;4(8):248–257.
[16] Letcher T, Waytashek M. Material property testing of 3D-printed specimen in PLA on an entry-level 3D printer. Proc ASME 2014 Int Mech Eng Congr Expo. Montreal, Quebec, Canada: ASME; 2014. https://doi.org/10.1115/IMECE2014-39379.
[17] ASTM-D638-14 Standard Test Method for Tensile Properties of Plastics. ASTM International; 2014.
[18] Dantec Dynamics A/S Q-400 DIC Standard 3D. Dantec Dynamics Turns Measurement into Knowledge. Dantec Dynamics A/S. https://www.dantecdynamics.com/q-400-dic
[19] Fottenburg WG. Some Applications of Holographic Interferometry. Exp Mech. 1969;8:281–5.
[20] Wang YY, Chen DJ, Chiang FP. Material testing by computer aided speckle interferometry. Exp Tech. 1993;17(5):30–2.
[21] Bastawros AF, Voloshin AS. Thermal Strain Measurements in Electronic Packages through Fractional Fringe Moiré Interferometry. J Electron Packag. 1990;112(4):303–8.
[22] Bruck HA, McNeil SR, Sutton MA, Peters WH. Digital Image Correlation Using Newton-Raphson Method of Partial Differential Correction. Exp Mech. 1989;29(3):261–7.
[23] Zhang D, Zhang X, Cheng G. Compression strain measurement by digital speckle correlation. Exp Mech. 1999;39(1):62–5.
[24] Sutton MA, Wolters WJ, Peters WH, Ranson WF, McNeil SR. Determination of Displacements using an improved Digital Correlation method. Image Vis Comput. 1983;1(3):133–9.
[25] Sutton MA, Cheng MQ, Peters WH, Chao YJ, McNeill SR. Application of an Optimized Digital Correlation Method to Planar Deformation Analysis. Image Vis Comput. 1986;4(3):143–51.
[26] Sutton MA, Turner JL, Bruck HA, Chae TA. Full-field Representation of Discretely Sampled Surface Deformation for Displacement and Strain Analysis. Exp Mech. 1991;31(2):168–77.
[27] Sutton MA, McNeill SR, Jang J, Babai M. Effects of Subpixel Image Restoration on Digital Correlation Error. Journal of Optical Engineering. 1988;27(10):870–7.
[28] Spagnolo G, Schirripa Paoletti D, Ambrosini D, Guattari G. Electro-optic correlation for in situ diagnostics in mural frescoes. *Pure &*

Applied Optics. Journal of the European Optical Society, Part A. 1997;6(5):557–63.
[29] Ackermann F. Photogrammetric Record, 11(64): 429-439 (October 1984) Digital Image Correlation: Performance and Potential Application in Photogrammetry. Photogramm Rec. 1984;11(64):429–39.
[30] Rippmann M, Lachauer L, Block P. Interactive vault design. Int J Space Structures. 2012;27(4):219–30.
[31] Manuello Bertetto A. Multi-body rope approach for grid shells: form-finding and imperfection sensitivity. Eng Struct. 2020;221:111029.
[32] Kilian A. Design exploration through bidirectional modeling of constraints. PhD thesis, MIT, Cambridge, MA; 2006.
[33] Tomlow J, Graefe R, Otto F, Szeemann H. The Model, Institute for Lightweight Structures (IL). University of Stuttgart; 1989.
[34] Burkhardt B, Bächer M. Multihalle Mannheim, Institute for Lightweight Structures (IL). University of Stuttgart; 1978.
[35] Chilton J, The Engineer's Contribution to Contemporary Architecture: Heinz Isler. London: Thomas Telford Press; 2000.
[36] Killian A, Ochsendorf J, Particle-spring system for structural form finding. J Int. Assoc. Shell Spatial Struct. 2005;45:147.
[37] Kuijvenhoven M, Hoogenboom PCJ. Particle–spring method for form-finding grid shell structures consisting of flexible members. J Int Assoc Shell Spatial Struct. 2012;53(1):171.
[38] Block P, Ochsendorf J, Trust network analysis: A new methodology for three dimensional equilibrium. J Int Assoc Shell Spatial Struct. 2007;48:155.
[39] Richardson JN, Adriaenssens S, Coelho RF, Bouillard P. Coupled Form Finding and Grid Optimization Approach for Single Layer Grid Shells. Eng Struct. 2013;52:230–9.
[40] Bazzucchi F, Manuello A, Carpinteri A. Instability load evaluation of shallow imperfection-sensitive structures by form and interaction parameters. Eur J Mech A, Solids. 2017;66:201–11.
[41] Bazzucchi F, Manuello A, Carpinteri A. Interaction between snap-through and Eulerian instability in shallow structures. Int J Nonlinear Mech. 2017;88:11–20.
[42] Carpinteri A, Bazzucchi F, Manuello A. Nonlinear instability analysis of long-span roofing structures: the case-study of Porta Susa railway-station. Eng Struct. 2016;110:48–58.
[43] Piana G, Lofrano E, Manuello A, Ruta G, Carpinteri A. Compressive buckling for symmetric TWB with non-zero warping stiffness. Eng Struct. 2017;135:246–58.
[44] Piana G, Lofrano E, Manuello A, Ruta G. Natural frequencies and buckling of compressed non-symmetric thin-walled beams. Thin-walled Struct. 2017;111:189–96.
[45] Carpinteri A, Malvano R, Manuello A, Piana G. Fundamental frequency evolution in slender beams subjected to imposed axial displacements. J Sound Vibrat. 2014;333(11):2390–403.
[46] Manuello A. Semi-Rigid Connection in Timber Structure: Stiffness Reduction and Instability Interaction. Int J Struct Stab Dyn. 2020;20(7):2050072.